Direct Imaging of Complex Nano- to Microscale Interfaces Involving Solid, Liquid, and Gas Phases

Konrad Rykaczewski,[†,‡,*] Trevan Landin,[§] Marlon L. Walker,[‡] John Henry J. Scott,[‡] and Kripa K. Varanasi[†,*]

[†]Department of Mechanical Engineering, Massachusetts Institute of Technology, Cambridge, Massachusetts 02139, United States, [‡]Material Measurement Laboratory, National Institute of Standards and Technology, Gaithersburg, Maryland 20899, United States, and [§]FEI Company, Hillsboro, Oregon 97124, United States

ABSTRACT

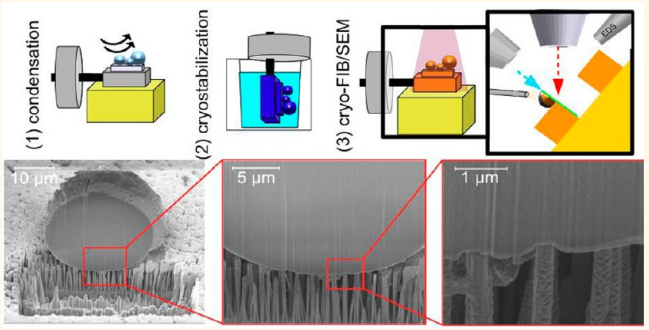

Surfaces with special wetting properties not only can efficiently repel or attract liquids such as water and oils but also can prevent formation of biofilms, ice, and clathrate hydrates. Predicting the wetting properties of these special surfaces requires detailed knowledge of the composition and geometry of the interfacial region between the droplet and the underlying substrate. In this work we introduce a 3D quantitative method for direct nanoscale visualization of such interfaces. Specifically, we demonstrate direct nano- to microscale imaging of complex fluidic interfaces using cryostabilization in combination with cryogenic focused ion beam milling and SEM imaging. We show that application of this method yields quantitative information about the interfacial geometry of water condensate on superhydrophilic, superhydrophobic, and lubricant-impregnated surfaces with previously unattainable nanoscale resolution. This type of information is crucial to a fundamental understanding as well as the design of surfaces with special wetting properties.

KEYWORDS: complex nanostructures · cryo-FIB/SEM · superhydrophobicity · lubricant-impregnated surfaces · nanoscale water condensation

Surfaces with special wetting properties have the potential to transform several industries, including power generation,[1−4] transportation,[5−8] water desalination,[9] gas and oil production,[10] and microelectronics thermal management.[1] Of particular interest are surfaces with extreme wetting properties, which are efficient at either repelling or attracting liquids such as water[11−19] and oils[20,21] but can also prevent formation of biofilms,[22,23] ice,[5−8,16,24,25] and clathrate hydrates.[10] The degree of surface wetting, typically measured by a drop's contact angle, depends on the balance of the products of corresponding interfacial surface areas and surface energies. From a theoretical perspective, the contact angle of a liquid interacting with a flat solid is predicted using Young's equation.[11,12,26,27] However, to achieve extreme wetting properties, the interfacial region between the droplet and the substrate must be structured and often contains an additional gas or liquid phase.[11] For example, nano- and/or microscale roughening of a flat hydrophobic substrate yields a superhydrophobic surface. Furthermore, the amount of air or intermediate liquid trapped between the topological features of such a surface determines what liquids are repelled by it[11,20,21,28,29] and whether drops of those liquids are in a "sticky" Wenzel state[28] or a "nonsticky" Cassie−Baxter state.[29] Predicting the wetting properties of these special surfaces using thermodynamics requires detailed knowledge of the composition and geometry of the interfacial region. Though there have been a few studies on static[30−36] and dynamic[3,19,37] aspects of the exterior three-phase contact line on textured surfaces, a quantitative method for direct nanoscale visualization of the three-dimensional droplet and substrate interface has not been developed. Light interference imaging works only in a few special cases involving smooth interfaces,[26,38,39] while light microscopy[40,41] and *in situ* small-angle X-ray scattering[42,43] can typically be used only to quantify the amount of air trapped between the topological features. Papadopoulos *et al.*[44] recently applied laser scanning confocal microscopy to image the shape of a water droplet with a diameter of a few millimeters deposited on a microstructured polymer surface. While promising, the need to stain the water droplet with a fluorescent dye and the 250 to 700 nm

* Address correspondence to konrad.rykaczewski@nist.gov; varanasi@mit.edu.

Received for review September 14, 2012 and accepted September 28, 2012.

Published online September 28, 2012
10.1021/nn304250e

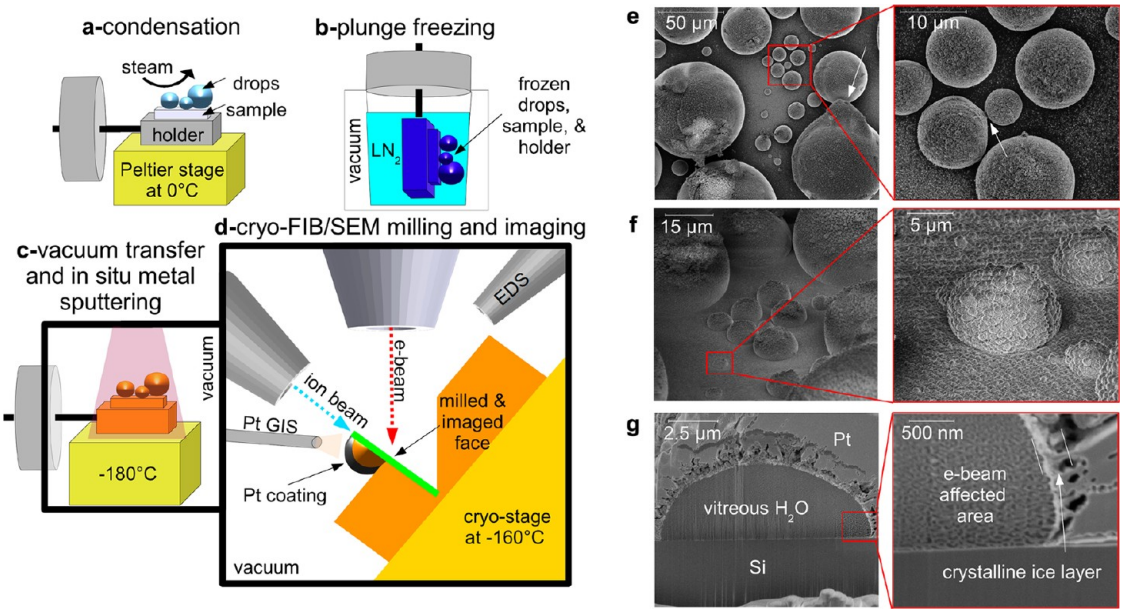

Figure 1. Step-by-step schematic of the cryo-FIB/SEM method: (a) water condensation on precooled sample, (b) rapid plunge freezing in liquid nitrogen slush (LN_2), (c) vacuum transfer and *in situ* conductive metal deposition, and (d) cryo-FIB/SEM milling and imaging; (e, f) top-down and 52° tilt SEM images of frozen water droplets that were condensed on a silicon wafer modified with a hydrophobic promoter coating; white arrows indicate freezing artifacts, and (g) 52° tilt cross-sectional images of the droplet highlighted in (f).

spatial resolution[44] do not allow for studies involving nanoscale topological features as well as water condensation. Water–solid interfaces can be directly imaged with nanoscale resolution using transmission mode of an environmental scanning electron microscope;[19,45,46] unfortunately, electron scattering limits applicability of this approach to submicrometer droplets.[46–48] Ensikat *et al.*[49] developed an interesting approach, in which droplets are frozen through contact with liquid nitrogen cooled superhydrophobic surfaces and, after careful "peeling off" of the substrate, are imaged using cryogenic scanning electron microscopy (cryo-SEM). However, this method works only for macroscopic droplets and is limited by a slow cooling rate, which results in the formation of crystalline ice and deformation of the geometry of the water droplet. Similarity, the freeze fracturing shadow casting cryo-SEM approach, developed by Isa *et al.*[50] to measure contact angles of solid particles on liquid–liquid interfaces, works only for liquid films and is not applicable to droplets. In this work, we demonstrate a direct method for nano- to microscale imaging of complex interfaces using cryostabilization, cryogenic focused ion beam (FIB) milling, and SEM imaging (cryo-FIB/SEM). Specifically, we show that microscale water droplets condensed on a variety of substrates retain their morphology during the nitrogen slush plunge freezing process and can be effectively cross-sectioned using FIB milling and imaged using SEM. We show examples of direct imaging of composite interfaces involving solid, liquid, and gas phases below water droplets condensed on silicon nanowire forests with hydrophilic and hydrophobic surface termination in the presence or absence of an intermediate water-repelling oil[18,24] with previously unattainable nanoscale resolution. We demonstrate that cryo-FIB/SEM is particularly suited for this application because of the advantages of secondary and backscatter electron imaging, energy dispersive spectrometry (EDS), and three-dimensional destructive tomography.

RESULTS AND DISCUSSION

In recent years cryo-FIB/SEM has become increasingly popular for cross-sectional imaging and TEM sample preparation of soft materials.[51–54] The first step of the process is cryostabilization of the sample, which is an established electron microscopy technique for preserving the geometry of hydrated biological[52,53,55] and geological[51] specimens as well as colloidal suspensions and emulsions.[56] The sample is first mounted to a metal stub and attached to a transfer holder. In our experiments, we encouraged water condensation on the sample by cooling the sample-holder assembly to about 0 °C using a Peltier element in the presence of moist air for about 2 min (Figure 1a).[3,57] Subsequently, we submerged the sample-holder assembly in liquid nitrogen slush for about 30 s, transported it under low-vacuum conditions into a high-vacuum transfer chamber, and coated it with a 10 to 20 nm conductive platinum layer at −180 °C (Figure 1b,c). The freezing rates during liquid nitrogen slush plunge freezing are on the order of 20 000 °C per second[58] and vitrify water microdroplets within a few microseconds.[59–63] Thus cryostabilization of the microdroplets was significantly

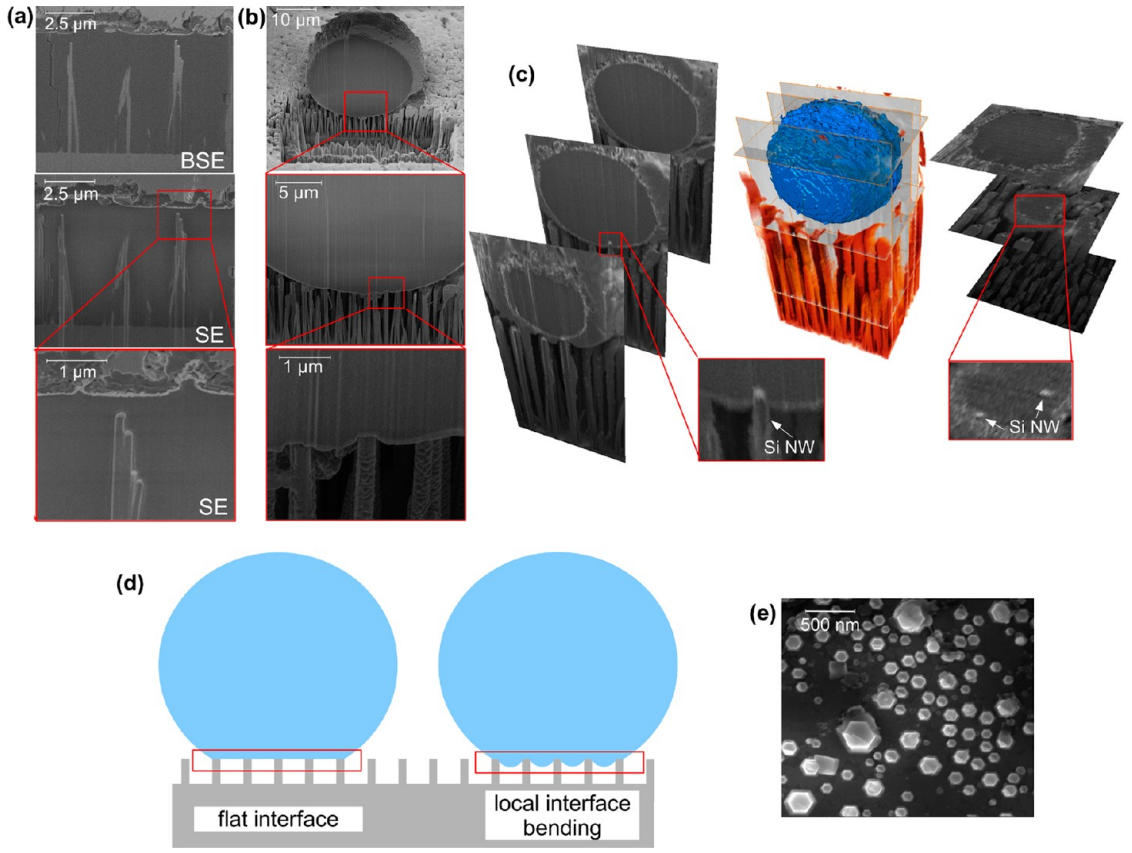

Figure 2. 52° tilt cryo-FIB/SEM images of water condensed on (a) superhydrophilic surface consisting of hydrophilic silicon nanowires (Si NW), (b) superhydrophobic surface consisting of Si NW coated with a hydrophobic promoter, (c) example of three-dimensional reconstruction of a droplet condensed on the superhydrophobic surface imaged using cryo-FIB/SEM tomography; example vertical and horizontal cross sections are also included, (d) schematic illustrating the difference between flat and locally bent droplet−substrate interface, and (e) top-down SEM image of FIB-cut Si NW section used to calculate the Si NW solid fraction.

faster than any changes of the droplet's geometry due to condensation[64−68] and evaporation,[69,70] which occur on a millisecond to second time scale in experimental conditions comparable to our procedure. Accordingly, most microdroplets condensed on a flat silicon wafer modified with a hydrophobic promoter retained their hemispherical shape during the plunge freezing process (Figure 1e,f). In some cases, we observed noticeable freezing artifacts such as minor deformation in the plunge direction and fusion of two droplets (Figure 1e,f). Importantly, we did not see evidence of water crystallization, which strongly deforms the geometry of the water droplets frozen through contact with liquid nitrogen cooled substrates.[49] During the transfer process, a 100 to 200 nm conformal ice layer formed, but did not affect visualization of the interface (Figure 1g). Once in the cryo-FIB/SEM chamber, the samples were exposed to a 10 to 20 s pulse of an organometallic gas containing platinum. The resulting few micrometer thick layer encapsulated most of the drop and, after a short curing using the ion beam, aided uniform milling during the cross-sectioning step.[53] The images in Figure 1g show that the subsequent FIB milling and SEM imaging clearly reveal the flat droplet and substrate interface. While the ion beam milling process is unlikely to cause thermal damage to vitreous ice,[52,71,72] we observed minor morphological changes to the cut water face due to prolonged high-magnification SEM imaging (Figure 1g). FIB milling of large droplets, which required large ion beam currents of several nanoamperes, resulted in formation of minor cracks within the frozen samples. We also observed that sample heating from prolonged sputtering and/or organometallic gas exposure can be significant and detrimental. This type of surface heating can result in selective sublimation of the frozen water, without affecting the outer layer, consisting of sputtered metal and deposited organometallic paste. As described in detail in the Methods section, careful adjustment of the process settings mitigates freezing and heating artifacts. We also note that while in this work we used a FIB with a gallium ion source, which is well suited for milling sub-150 μm objects, the cryostabilization process is compatible with the newer plasma source FIBs, which can easily cut through significantly larger objects.[73]

We investigated the interfacial geometry of water condensing out of air onto a silicon nanowire forest

with hydrophilic and hydrophobic surface terminations. We first examined water condensation on the as-grown nanowires, which contain a thin hydrophilic native oxide layer. The cross-sectional images in Figure 2a show that condensation on this superhydrophilic surface results in formation of a uniform film of water. Imaging of this cross-section was instructive, as it highlights the difference between imaging in secondary (SE) and backscattered (BSE) electron modes. Specifically, by imaging in the BSE mode, we observed a much stronger contrast between the silicon nanowires, their gold nanoparticle top, and the liquid. Second, we demonstrated that condensation on the silicon nanowire forest modified with perfluorinated silane produced dramatically different results. After chemical modification, the surface became superhydrophobic and condensing water formed nearly spherical microdroplets. The SEM images of this interface show that the droplet is in a nonwetting Cassie–Baxter state and has a contact angle above 170° (Figure 2b). The single cross section shows that the droplet sits on top of the nanowires and that only submicroscopic bending of the liquid surface occurs in the vicinity of the nanostructures. We obtained significantly more quantitative information about the interface through FIB/SEM tomography of the drop. This three-dimensional visualization technique is often referred to as destructive tomography because the object of interest is gradually sliced away during serial FIB milling and SEM imaging. After alignment, resampling, and segmentation of an acquired set of images, the entire object as well as arbitrary planar cross sections in any orientation can be reconstructed from the volumetric data set. Results of this procedure are illustrated in Figure 2c and Movie 1, containing example vertical and horizontal cross sections as well as a full three-dimensional reconstruction of a ~7.5 μm diameter droplet condensed on the nanowires. The surface of this droplet is in contact with 11 nanowires, of which only one penetrates the liquid to a depth of 460 ± 30 nm. The most pronounced bending of the liquid interface in the vicinity of a nanowire has a radius of curvature of about 650 nm. Using the volumetric data set we quantified the total liquid–air, base liquid–air, and liquid–solid interfacial areas as approximately 176, 30, and 1 μm^2, respectively (the base liquid–air area was assumed to be the surface area of the liquid below the horizontal plane that passes the highest nanowire-liquid intersection point). Cassie and Baxter[26,29] related the apparent contact angle, θ^*, to the flat surface's contact angle, θ, and to the solid area fraction, f, through

$$\cos\theta^* = f(1+\cos\theta) - 1 \quad (1)$$

We compared predictions of eq 1 for the idealized case of a flat interface, often assumed in the literature,[12,14,21,29,74] and our directly measured values quantifying the local interface bending around the nanowires (see Figure 2d). For both of the cases we used θ = 104°, which is the experimentally measured value of contact angle of a silicon wafer surface modified with the perfluorinated silane (see Methods section for further details). We estimated f = 0.27 for the flat interface case by measuring the fraction of the substrate area occupied by the base of horizontally FIB-cut nanowires (see Figure 2e).[3] Substituting the θ and the f values for the flat interface case into eq 1 yields a significantly underpredicted value of θ^* = 143°. In turn, substituting our directly measured value of f = 1/30 into eq 1 we obtained θ^* = 169°, which is in close agreement with both the θ^* = 167.5° macroscopic contact angle measured using a goniometer and the $\theta^* \approx$ 170° microscopic contact angle estimated from the volumetric data set.

We also investigated the interfacial geometry of four-phase lubricant-impregnated surfaces[24,75] (such hybrid liquid–solid surfaces have also been referred to as hemisolid and hemiliquid,[11] slippery presuffused surfaces,[17] and slippery liquid infused porous

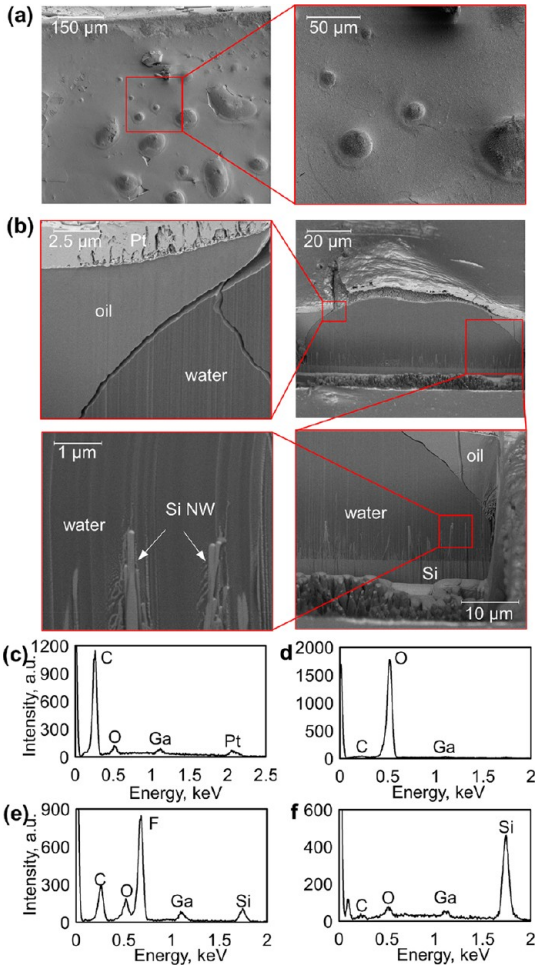

Figure 3. (a, b) Top-down and 52° tilt cross-sectional images of water droplets condensed on hydrophilic Si NW impregnated with oil and EDS spectra of (c) Pt coating, (d) water drop, (e) oil-impregnated Si NW, and (f) Si substrate. All cross-sectional imaging is performed in the BSE mode.

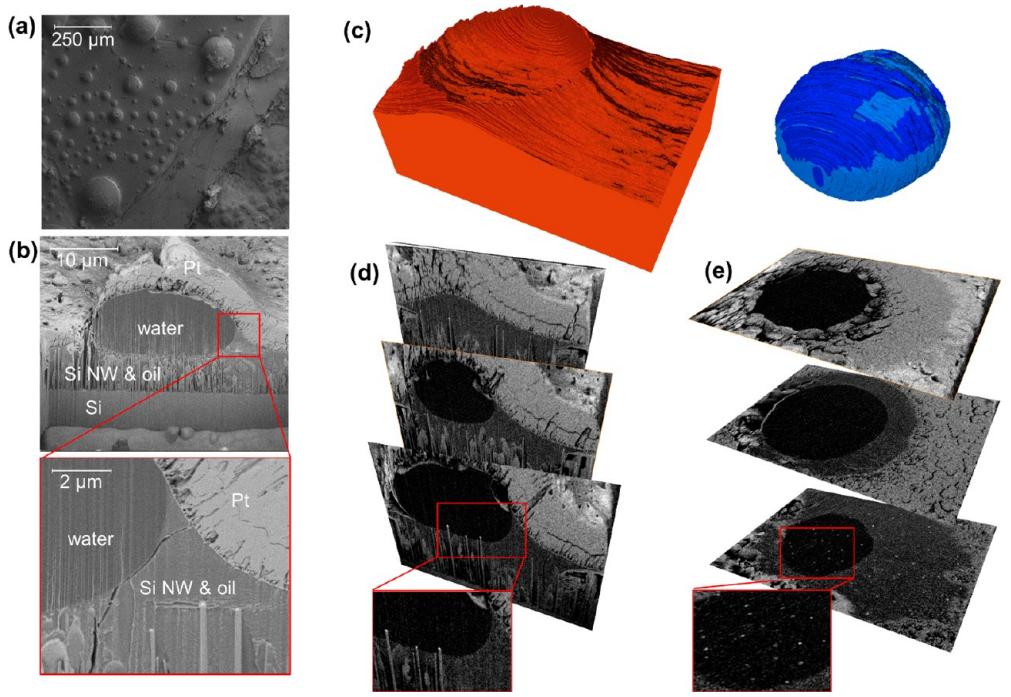

Figure 4. (a) Top-down images, (b) 52° tilt cross-sectional images, (c) 3D reconstruction obtained using cryo-FIB/SEM tomography, and (d) vertical and (e) horizontal cross sections of a water lens condensed on hydrophobic silicon nanowires impregnated with oil; in (c) the water lens is separated from the LIS surface to clearly show the oil meniscus. The darker shade of blue on the surface of the drop indicates the location of minor voids formed during sample preparation. All cross-sectional imaging is performed in the BSE mode.

surfaces[16,25]), which consisted of air, water, oil, and a nanostructured solid. In particular, we studied the wetting characteristics of condensed water droplets on superhydrophilic and superhydrophobic silicon nanowire surfaces impregnated with oil, which is immiscible with water (we refer to these surfaces as LIS-1 and LIS-2 hereafter). Top-down SEM images in Figure 3a show that on LIS-1 only some microdroplets with diameters below 75 μm appear to have a circular circumference, while all larger drops have irregular shapes. Interestingly, the cross section shown in Figure 3b reveals that the shape observed from the top-down perspective is only the exposed tip of a larger subsurface droplet. The droplet emerges at most 10 μm above the planar air–liquid interface with an apparent diameter of about 65 μm. At its true base, located about 25 μm below the planar air–liquid interface, the drop has a diameter of about 100 μm. We used EDS elemental analysis to identify each observed phase in the cross section. The acquired spectra are presented in Figure 3c–f. As expected, the top layer consisted primarily of carbon, oxygen, and platinum and corresponded to the protective conductive coating (Figure 3c).[76] The drop, which penetrated all the way to the bottom of the nanowires layer, consisted predominantly of oxygen and is relatively free of carbon, and thus corresponded to water (Figure 3d). The second fluid phase showed strong carbon, oxygen, and fluorine signals and was identified as vacuum oil (Figure 3e). The fluorine signal came from the polytetrafluoroethylene particles, which are contained within the vacuum oil (this spectrum also contains a silicon signal because it corresponds to the liquid layer between the nanowires in Figure 4b; see Methods section). As expected, the spectrum of the silicon substrate primarily consisted of silicon. We note that all layers included trace gallium as well as carbon and oxygen signals due to ion implantation and material redeposition during milling. Thus, our imaging method confirmed that LIS-1 is unstable,[16,17] and condensing water droplets can entirely substitute for the oil film encapsulating the hydrophilic nanowires.

Coating of the nanowires with the hydrophobic promoter prior to impregnation with the oil produced a stable LIS, consistent with previously reported studies.[16,17,25] Water condensation on this surface led to formation of droplets, which, from a top-down perspective, had circular circumferences for all size ranges (Figure 4a). Cross-sectioning such droplets clearly revealed floating lens-type geometry and formation of an oil meniscus near the drop edge (Figure 4b–e). The three-dimensional reconstruction of the oil–nanowire layer shown in Figure 4c and Movie 2, obtained through FIB/SEM tomography and image processing, shows the crater-like geometry of this meniscus with internal and external radii of curvature of about 2.5 and 5 μm, respectively. In turn, the water lens has a height and

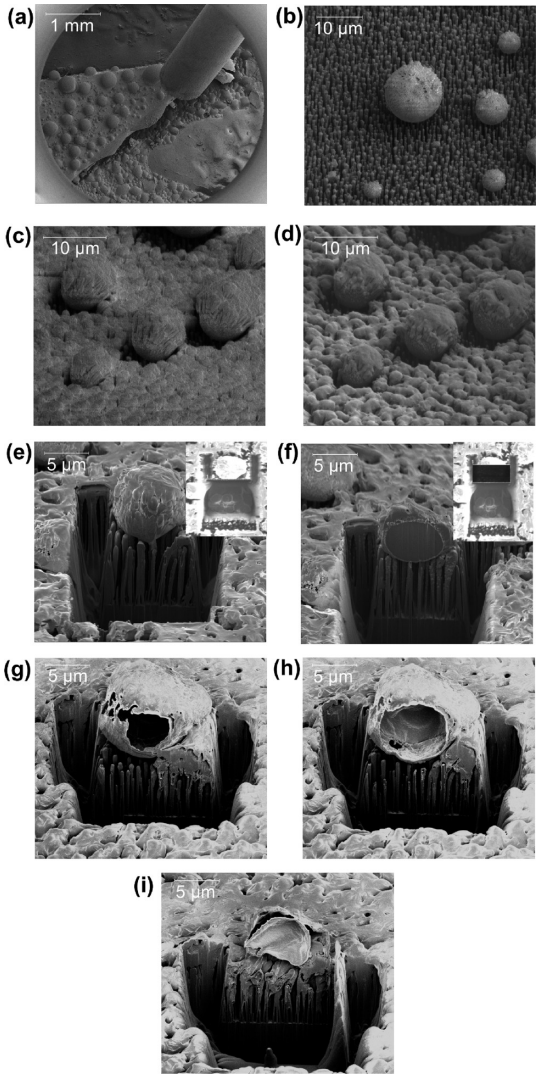

Figure 5. (a) Low-magnification view of the sample and GIS needle during Pt deposition. (b−f) Example of typical cryo-FIB/SEM imaging procedure: (b) frozen droplets on the superhydrophobic nanowires, (c) droplets covered with frozen Pt layer, (d) same droplets after ion beam curing of the Pt layer, (e, f) images of droplet with FIB milled three-side trench (e) before and (f) during slice-and-view imaging (the insets in top right corner show the FIB view). (g−i) Progressive cross sections through a hollow droplet shell.

diameter of about 9 and 15 μm, respectively. The vertical and planar cross sections in Figure 4d,e clearly show that the water lens is penetrated by significantly more nanowires than the droplet condensed on the superhydrophobic surface. Specifically, the lens surface is in contact with 70 nanowires, of which 32 penetrate the water surface to an average and a maximum depth of 478 $\pm$ 230 and 930 $\pm$ 63 nm, respectively. As in the case of the superhydrophobic surface, we observed local interface bending in the vicinity of the nanowires with a typical radius of curvature of 500 to 1500 nm. Furthermore, using the volumetric data set we quantified the total water−air, water−oil, and water−solid contact areas as approximately 485, 476, and 9 μm^2, respectively. We did not attempt to use these values to predict the contact angle, as a theoretical understanding of LIS is just beginning to emerge.[24,77] Lastly, we note that in the case of the stable LIS-2 surface significantly more interactions between the solid and water phases were observed than in the case of the superhydrophobic surface.

CONCLUSIONS

In conclusion, in this work we demonstrated two- and three-dimensional direct nano- to microscale imaging of complex fluidic interfaces on silicon nanowire forests with varied wetting properties using cryostabilization in combination with cryo-FIB/SEM. We showed that application of this method yields quantitative information about the interfacial areas of water condensate on superhydrophilic, superhydrophobic, and lubricant-impregnated surfaces with previously unattainable nanoscale resolution. For the case of the superhydrophobic silicon nanowire surface, we demonstrated that the Cassie−Baxter equation yields a much more accurate prediction of the drop's contact angle with substitution of the directly measured interfacial areas rather than the estimates based on the typically used flat interface assumption. The nanoscale resolution quantitative information about the interfacial region attainable using our method is crucial to a fundamental understanding as well as the design of surfaces with special wetting properties.

METHODS

Cryo-FIB FIB/SEM Procedure. The low-temperature experiments were carried out using an FEI Nova Nanolab 600 Dual Beam[78] equipped with a Quorum PP2000T cryo-transfer system and an INCA XMax 80 mm^2 SDD EDS detector (Oxford, Abingdon, Oxfordshire, U.K.). Three to four ~3 mm by ~3 mm samples were attached to a 10 mm diameter copper stub using double-sided carbon tape and placed in a brass cryo-stage holder. The sample-holder assembly was cooled to about 0 °C using a 1.2 cm by 1.2 cm Analog Technologies thermoelectric cooler module mounted to a 2.5 cm × 5 cm × 5 cm aluminum heat sink for a period of 2 min. Rapid water condensation was encouraged by placing an open cup of nearly boiling water in the vicinity of the sample-holder assembly, which locally provided a source of warm and moist air. Subsequently, the samples were submerged into liquid nitrogen slush, which was made by partially evacuating a chamber containing liquid nitrogen. After about 30 s, when bubble formation around the sample terminated, the freezing chamber was evacuated. Next, the samples were moved to the transfer chamber under vacuum. The chamber was pre-evacuated to a pressure of 10^{-3} to 10^{-2} Pa and precooled to a temperature of −180 to −190 °C. *In situ* conductive metal deposition was achieved by plasma sputtering in an argon gas environment with a 5 mA

current. To minimize potential heating effects, sputtering was done in three 30 s periods with 60 s breaks in between. Subsequently the coated samples were transferred directly into the FIB/SEM chamber, which had a stage and decontamination coldfinger precooled to −150 to −160 °C and −180 to −190 °C, respectively. Prior to FIB milling, the samples were exposed to a 10 to 20 s pulse of a $C_9H_{16}Pt$ gas precursor at 28 °C, which was introduced into the microscope chamber using a built-in gas injection system (GIS). Specifically, the gas was introduced through a 500 μm inner diameter needle that was placed about 500 μm above the sample (Figure 5a). During the exposure the gas froze to the surface, resulting in about a 1 to 2 μm amorphous layer encapsulating most of the drops (see difference between Figure 5b and c). Because this layer was initially electrically insulating, it was cured using a short exposure to the ion beam at 30 keV, 0.92 nA, and 100 ns dwell time per pixel. The time of the exposure varied depending on the sample and region of interest and was adjusted based on morphological changes of the platinum layer (*i.e.*, change from choppy to smooth; see difference between Figure 5 c and d). This additional coating prevented shape distortion due to direct ion beam exposure and indirect effects such as material redeposition as well as aided uniform milling during the cross-sectioning step.[53] The above-described sample preparation procedure mitigated detrimental heating effects, which can result in formation of significant voids in the ice and, in extreme cases, nearly hollow spherical shells made of the organometallic coating (see Figure 5g−i). For example, in the case of the water lens illustrated in Figure 4c, only about 13% of the ice volume was replaced by voids.

FIB milling was performed with normal incidence of the ion beam (sample tilt of 52° to 53°) and at an ion beam energy of 30 keV, an ion current of 0.48 to 21 nA, and a dwell time of 1 μs per pixel. The structure cross sections were obtained by FIB milling 10 to 50 μm deep trenches at an ion beam current of 9.3 to 21 nA. Subsequently the surfaces were polished at 0.48 to 2.6 nA. Serial milling and imaging was performed using FEI's Auto Slice and View tool with a slice thickness of 100 nm. For three-dimensional visualization, the collected images were aligned, resampled, and semiautomatically segmented using Avizo 7 Fire software from VSG. All structures were imaged at 0° and 52° tilt in the objective lens immersion mode using either secondary or backscattered electrons with electron beam energies of 1 to 2 keV and an electron beam current of 13 to 120 pA. To collect the EDS spectra, electron beam energy and current were increased to 3 keV and 1.1 nA, respectively. All reported distance values are averages of six independent measurements, and the associated uncertainty is expressed with a coverage factor of 1. We note that quantification of the uncertainty of the surface areas estimated from the volumetric data set is quite challenging and is not attempted in this work. Thus, we report only approximate area values.

Material Preparation. The silicon nanowires with diameters between 50 and 200 nm and height of about 8.6 μm were grown in a custom-designed horizontal hot-walled chemical vapor deposition system at 850 °C using a $SiCl_4/H_2/N_2$ gaseous mixture. The vapor−liquid−solid (VLS) growth was catalyzed by gold nanoparticles formed on a Si(111) substrate by annealing a 5 nm thick gold (Au) film. Further details of the nanowire growth can be found elsewhere.[79] The as-grown nanowires with a native oxide outer layer were referred to as hydrophilic. To produce the hydrophobic and superhydrophobic surfaces, flat silicon wafers and the silicon nanowire forests were modified with a hydrophobic promoter. Specifically, the surfaces were first rinsed using 2-propanol and cleaned using UV ozone for approximately 15 min to remove the adventitious hydrocarbon. After cleaning and subsequent rinsing with 2-propanol, samples were blown dry with nitrogen and placed in a desiccator, which was purged using dry N_2 and evacuated with roughing vacuum. Monolayer formation on the wafers by vapor deposition was accomplished by exposure to 1*H*,1*H*,2*H*,2*H*-perfluorodecyltrichlorosilane (Alfa Aesar) in the desiccator under vacuum for 24 to 48 h. To fabricate the LIS, the edge of the nanowire sample was put in contact with a small drop[17] of 25/6 Fomblin LVAC diffusion pump oil. To prevent an excess oil layer from forming on top of the nanowires, the oil wicking process was monitored using a light microscope. The macroscopic water contact angles of the hydrophobic, superhydrophobic, and LIS-2 surfaces were 104 ± 4°, 167.5 ± 3.5°, and 114 ± 1°, respectively. Water droplets began to slide from the LIS-2 surface when the surface was tilted to about 10°. The water contact angle on both the superhydrophilic and LIS-1 surfaces was below 5°.

Conflict of Interest: The authors declare no competing financial interest.

Acknowledgment. The authors also kindly acknowledge Dr. Albert Davydov and Dr. Sergiy Krylyuk from NIST for providing the VLS silicon nanowire samples, Dr. Andras E. Vladar from NIST for lending spare parts of the cryo-system, Bob Casey from FEI for help with the Nova Nanolab FIB/SEM system, and Dr. John Pettibone from NIST for insightful comments on the manuscript. K.K.V. gratefully acknowledges the NSF Career Award (0952564) and the Dupont-MIT Alliance for funding this work.

Supporting Information Available: Movies of three-dimensional reconstructions of water droplets condensed on the superhydrophobic and LIS-2 surfaces acquired using cryo-FIB/SEM destructive tomography are available free of charge via the Internet at http://pubs.acs.org.

REFERENCES AND NOTES

1. Dietz, C.; Rykaczewski, K.; Fedorov, A. G.; Joshi, Y. Visualization of Droplet Departure on a Superhydrophobic Surface and Implications to Heat Transfer Enhancement During Dropwise Condensation. *Appl. Phys. Lett.* **2010**, *97*, 033104.
2. Chen, R.; Lu, M.-C.; Srinivasan, V.; Wang, Z.; Cho, H. H.; Majumdar, A. Nanowires for Enhanced Boiling Heat Transfer. *Nano Lett.* **2009**, *9*, 548–553.
3. Rykaczewski, K.; Chinn, J.; Walker, L. A.; Scott, J. H. J.; Chinn, A. M.; Jones, W.; Hao, C.; Yao, S.; Wang, Z. How Nanorough Is Rough Enough to Make a Surface Superhydrophobic During Condensation? *Soft Matter* **2012**, *8*, 8786–8794.
4. Varanasi, K. K.; Hsu, M.; Bhate, N.; Yang, W.; Deng, T. Spatial Control in the Heterogeneous Nucleation of Water. *Appl. Phys. Lett.* **2009**, *95*, 094101.
5. Varanasi, K. K.; Deng, T.; Smith, J. D.; Hsu, M.; Bhate, N. Frost Formation and Ice Adhesion on Superhydrophobic Surfaces. *Appl. Phys. Lett.* **2010**, *97*, 234102.
6. Mishchenko, L.; Hatton, B.; Bahadur, V.; Taylor, J. A.; Krupenkin, T.; Aizenberg, J. Design of Ice-Free Nanostructured Surfaces Based on Repulsion of Impacting Water Droplets. *ACS Nano* **2010**, *4*, 7699–7707.
7. Meuler, A. J.; Smith, J. D.; Varanasi, K. K.; Mabry, J. M.; McKinley, G. H.; Cohen, R. E. Relationships between Water Wettability and Ice Adhesion. *ACS Appl. Mater. Interfaces* **2010**, *2*, 3100–3110.
8. Meuler, A. J.; McKinley, G. H.; Cohen, R. E. Exploiting Topographical Texture to Impart Icephobicity. *ACS Nano* **2010**, *4*, 7048–7052.
9. Humplik, T.; Lee, J.; O'Hern, S. C.; Fellman, B. A.; Baig, M. A.; Hassan, S. F.; Atieh, M. A.; Rahman, F.; Laoui, T.; Karnik, R.; *et al*. Nanostructured Materials for Water Desalination. *Nanotechnol.* **2011**, *22*, 292001.
10. Smith, J. D.; Meuler, A. J.; Bralower, H. L.; Venkatesan, R.; Subramanian, S.; Cohen, R. E.; McKinley, G. H.; Varanasi, K. K. Hydrate-Phobic Surfaces: Fundamental Studies in Clathrate Hydrate Adhesion Reduction. *Phys. Chem. Chem. Phys.* **2012**, *14*, 6013–6020.
11. Quéré, D. Non-Sticking Drops. *Rep. Prog. Phys.* **2005**, *68*, 2495–2532.
12. Quéré, D. Wetting and Roughness. *Ann. Rev. Mater. Res.* **2008**, *38*, 71–99.
13. Roach, P.; Shirtcliffe, N. J.; Newton, M. I. Progess in Superhydrophobic Surface Development. *Soft Matter* **2008**, *4*, 224–240.
14. Nosonovsky, M.; Bhushan, B. Biomimetic Superhydrophobic Surfaces: A Multiscale Approach. *Nano Lett.* **2007**, *7*, 2633–2637.

15. Dorrer, C.; Ruhe, J. Wetting of Silicon Nanograss: From Superhydrophilic to Superhydrophobic Surfaces. *Adv. Mater.* **2008**, *20*, 159–163.
16. Wong, T.-S.; Kang, S. H.; Tang, S. K. Y.; Smythe, E. J.; Hatton, B. D.; Grinthal, A.; Aizenberg, J. Bioinspired Self-Repairing Slippery Surfaces with Pressure-Stable Omniphobicity. *Nature* **2011**, *477*, 443–447.
17. Lafuma, A.; Quéré, D. Slippery Pre-Suffused Surfaces. *Europhys. Lett.* **2011**, *96*, 56001.
18. Rykaczewski, K.; Scott, J. H. J.; Rajauria, S.; Chinn, J.; Chinn, A. M.; Jones, W. Three Dimensional Aspects of Droplet Coalescence During Dropwise Condensation on Superhydrophobic Surfaces. *Soft Matter* **2011**, *7*, 8749–8752.
19. Rykaczewski, K. Microdroplet Growth Mechanism During Water Condensation on Superhydrophobic Surfaces. *Langmuir* **2012**, *28*, 7720–7729.
20. Tuteja, A.; Choi, W.; Mabry, J. M.; McKinley, G. H.; Cohen, R. E. Robust Omniphobic Surfaces. *Proc. Natl. Acad. Sci. U. S. A.* **2008**, 18200–18205.
21. Tuteja, A.; Choi, W.; Ma, M.; Mabry, J. M.; Mazzella, S. A.; Rutledge, G. C.; McKinley, G. H.; Cohen, R. E. Designing Superoleophobic Surfaces. *Science* **2007**, *318*, 1618–1622.
22. Genzer, J.; Efimenko, K. Recent Developments in Superhydrophobic Surfaces and Their Relevance to Marine Fouling: A Review. *Biofouling* **2006**, *22*, 339–360.
23. Epstein, A. K.; Wong, T.-S.; Belisle, R. A.; Boggs, E. M.; Aizenberg, J. Liquid-Infused Structured Surfaces with Exceptional Anti-Biofouling Performance. *Proc. Natl. Acad. Sci. U. S. A.* **2012**, *109*, 13182–13187.
24. Smith, J. D.; Dhiman, R.; Varanasi, K. K. Liquid-Encapsulating Surfaces: Overcoming the Limitations of Superhydrophobic Surfaces for Robust Non-Wetting and Anti-Icing Surfaces. *Bull. Am. Phys. Soc.* **2011**, *56*, http://meetings.aps.org/link/BAPS.2011.DFD.S4.1.
25. Kim, P.; Wong, T.-S.; Alvarenga, J.; Kreder, M. J.; Adorno-Martinez, W. E.; Aizenberg, J. Liquid-Infused Nanostructured Surfaces with Extreme Anti-Ice and Anti-Frost Performance. *ACS Nano* **2012**, *6*, 6569–6577.
26. de Gennes, P.-G.; Brochard-Wyart, F.; Quéré, D. *Capillarity and Wetting Phenomena: Drops, Bubbles, Pearls, Waves*; Springer: New York, 2003.
27. Israelachvili, J. N. *Intermolecular and Surface Forces*, 3rd ed.; Elsevier: San Diego, 2011.
28. Wenzel, R. N. Resistance of Solids Surfaces to Wetting by Water. *Ind. Eng. Chem.* **1936**, *28*, 988–994.
29. Cassie, A. B. D.; Baxter, S. Wettability of Porous Surfaces. *Trans. Faraday Soc.* **1944**, *40*, 546–551.
30. Lv, C.; Yang, C.; Hao, P.; He, F.; Zheng, Q. Sliding of Water Droplets on Microstructured Hydrophobic Surfaces. *Langmuir* **2010**, *26*, 8704–8708.
31. Priest, C.; Albrecht, T. W. J.; Sedev, R.; Ralston, J. Asymmetric Wetting Hysteresis on Hydrophobic Microstructured Surfaces. *Langmuir* **2009**, *25*, 5655–5660.
32. Choi, W.; Tuteja, A.; Mabry, J. M.; Cohen, R. E.; McKinley, G. H. A Modified Cassie–Baxter Relationship to Explain Contact Angle Hysteresis and Anisotropy on Non-Wetting Textured Surfaces. *J. Colloid Interface Sci.* **2009**, *339*, 208–216.
33. Krumpfer, J. W.; Bian, P.; Zheng, P.; Gao, L.; McCarthy, T. J. Contact Angle Hysteresis on Superhydrophobic Surfaces: An Ionic Liquid Probe Fluid Offers Mechanistic Insight. *Langmuir* **2011**, *27*, 2166–2169.
34. Dufour, R.; Brunet, P.; Harnois, M.; Boukherroub, R.; Thomy, V.; Senez, V. Zipping Effect on Omniphobic Surfaces for Controlled Deposition of Minute Amounts of Fluid or Colloids. *Small* **2012**, *8*, 1229–1236.
35. Dufour, R.; Harnois, M.; Thomy, V.; Boukherroub, R.; Senez, V. Contact Angle Hysteresis Origins: Investigation on Super-Omniphobic Surfaces. *Soft Matter* **2011**, *7*, 9380–9387.
36. Bormashenko, E.; Bormashenko, Y.; Stein, T.; Whyman, G.; Pogreb, R.; Barkay, Z. Environmental Scanning Electron Microscopy Study of the Fine Structure of the Triple Line and Cassie–Wenzel Wetting Transition for Sessile Drops Deposited on Rough Polymer Substrates. *Langmuir* **2007**, *23*, 4378–4382.
37. Paxson, A. T.; Varanasi, K. K. Direct Observation of Hierarchical Contact Line Depinning. *Bull. Am. Phys. Soc.* **2011**, *56*, http://meetings.aps.org/link/BAPS.2011.DFD.S26.2.
38. Driscoll, M. M.; Nagel, S. R. Ultrafast Interference Imaging of Air in Splashing Dynamics. *Phys. Rev. Lett.* **2011**, *107*, 154502.
39. de Ruiter, J.; Oh, J. M.; van den Ende, D.; Mugele, F. Dynamics of Collapse of Air Films in Drop Impact. *Phys. Rev. Lett.* **2012**, *108*, 074505.
40. Ma, X.; Wang, S.; Lan, Z.; Peng, B.; Ma, H. B.; Cheng, P. Wetting Mode Evolution of Steam Dropwise Condensation on Superhydrophobic Surface in the Presence of Noncondensable Gas. *J. Heat Transfer* **2012**, *134*, 021501.
41. Narhe, R. D.; Beysens, D. A. Growth Dynamics of Water Drops on a Square-Pattern Rough Hydrophobic Surface. *Langmuir* **2007**, *23*, 6486–6489.
42. Cho, J. K. L.; Palmer, L. A.; Wu, A. H.-F.; Liaw, I. I.; Cookson, D.; Lamb, R. N. *In Situ* Saxs Analysis of Interfacial Wetting on Nanorough Surfaces. *Aust. J. Chem.* **2012**, *65*, 254–258.
43. Wu, A. H. F.; Cho, K. L.; Liaw, I. I.; Moran, G.; Kirby, N.; Lamb, R. N. Hierarchical Surfaces: An *in Situ* Investigation into Nano and Micro Scale Wettability. *Faraday Discuss.* **2010**, *146*, 223–232.
44. Papadopoulos, P.; Deng, X.; Mammen, L.; Drotlef, D. M.; Battagliarin, G.; Li, C.; Müllen, K.; Landfester, K.; del Campo, A.; Butt, H. J.; *et al*. Wetting on the Microscale: Shape of a Liquid Drop on a Microstructured Surface at Different Length Scales. *Langmuir* **2012**, *28*, 8392–8398.
45. Rykaczewski, K.; Scott, J. H. J.; Fedorov, A. G. Electron Beam Heating Effects During Environmental Scanning Electron Microscopy Imaging of Water Condensation on Superhydrophobic Surfaces. *Appl. Phys. Lett.* **2011**, *98*, 093106.
46. Rykaczewski, K.; Scott, J. H. J. Methodology for Imaging Nano-to-Microscale Water Condensation Dynamics on Complex Nanostructures. *ACS Nano* **2011**, *5*, 5926–5968.
47. Barkay, Z. Wettability Study Using Transmitted Electrons in Environmental Scanning Electron Microscope. *Appl. Phys. Lett.* **2010**, *96*, 183109.
48. Barkay, Z. Dynamic Study of Nanodroplet Nucleation and Growth on Self-Supported Nanothick Liquid Films. *Langmuir* **2011**, *26*, 18581–18584.
49. Ensikat, H. J.; Schulte, A. J.; Koch, K.; Barthlott, W. Droplets on Superhydrophobic Surfaces: Visualization of the Contact Area by Cryo-Scanning Electron Microscopy. *Langmuir* **2009**, *25*, 13077–13083.
50. Isa, L.; Lucas, F.; Wepf, R.; Reimhult, E. Measuring Single-Nanoparticle Wetting Properties by Freeze-Fracture Shadow-Casting Cryo-Scanning Electron Microscopy. *Nat. Commun.* **2011**, *2*, 438.
51. Desbois, G.; Urai, J. L.; Burkhardt, C.; Drury, M. R.; Hayles, M.; Humbel, B. Cryogenic Vitrification and 3D Serial Sectioning Using High Resolution Cryo-Fib SEM Technology for Brine-Filled Grain Boundaries in Halite: First Results. *Geofluids* **2008**, *8*, 60–72.
52. Marko, M.; Hsieh, C.; Schalek, R.; Frank, J.; Mannella, C. Focused-Ion-Beam Thinning of Frozen-Hydrated Biological Specimens for Cryo-Electron Microscopy. *Nat. Methods* **2007**, *4*, 215–217.
53. Hayles, M. F.; Stokes, D. J.; Phifer, D.; Findlay, K. C. A Technique for Improved Focused Ion Beam Milling of Cryo-Prepared Life Science Specimens. *J. Microsc.* **2007**, *226*, 263–269.
54. Winter, D. A. M. D.; Schneijdenberg, C. T. W. M.; Lebbink, M. N.; Lich, B.; Verkleij, A. J.; Drury, M. R.; Humbel, B. M. Tomography of Insulating Biological and Geological Materials Using Focused Ion Beam (FIB) Sectioning and Low-kV BSE Imaging. *J. Microsc.* **2009**, *233*, 372–383.
55. Dobro, M. J.; Melanson, L. A.; Jensen, G. J.; McDowall, A. W. Plunge Freezing for Electron Cryomicroscopy. *Meth. Enzymol.* **2010**, *481*, 63–82.
56. Binks, B. P.; Kirkland, M. Interfacial Structure of Solid-Stabilised Emulsions Studied by Scanning Electron Microscopy. *Phys. Chem. Chem. Phys.* **2002**, *4*, 3727–3733.

57. Rykaczewski, K.; Chinn, J.; Walker, M. L.; Scott, J. H. J.; Chinn, A.; Jones, W. Dynamics of Nanoparticle Self Assembly into Superhydrophobic Liquid Marbles During Water Condensation. *ACS Nano* **2011**, *5*, 9746–9754.
58. Dykstra, M. J.; Reuss, L. E. *Biological Electron Microscopy: Theory, Techniques, and Troubleshooting*; Springer: New York, 2003.
59. Dubochet, J. The Physics of Rapid Cooling and Its Implications for Cryoimmobilization of Cells. In *Methods in Cell Biology*; McIntosh, J. R., Ed.; Academic Press: New York, 2007; pp 7−21.
60. Bruggeller, P.; Mayer, E. Complete Vitrification in Pure Liquid Water and Dilute Aqueous Solutions. *Nature* **1980**, *288*, 569–571.
61. Zasadzinski, J. A. N. A New Heat Transfer Model to Predict Cooling Rates for Rapid Freezing Fixation. *J. Microsc.* **1988**, *150*, 137–149.
62. Lepault, J.; Bigot, D.; Studer, D.; Erk, I. Freezing of Aqueous Specimens: An X-Ray Diffraction Study. *J. Microsc.* **1997**, *187*, 158–166.
63. Dubochet, J.; McDowall, A. W. Vitrification of Pure Water for Electron Microscopy. *J. Microsc.* **1981**, *124*, 3–4.
64. Beysens, D.; Knobler, C. M. Growth of Breath Figures. *Phys. Rev. Lett.* **1986**, *57*, 1433–1436.
65. Viovy, J. L.; Beysens, D.; Knobler, C. M. Scaling Description for the Growth of Condensation Patterns on Surfaces. *Phys. Rev. A* **1988**, *37*, 4965–4970.
66. Fritter, D.; Knobler, C. M.; Beysens, D. A. Experiments and Simulation of the Growth of Droplets on a Surface (Breath Figures). *Phys. Rev. A* **1991**, *43*, 2858–2869.
67. Narhe, R. D.; Beysens, D. A. Water Condensation on a Super-Hydrophobic Spike Surface. *Europhys. Lett.* **2006**, *75*, 98–104.
68. Narhe, R. D.; González-Viñas, W.; Beysens, D. A. Water Condensation on Zinc Surfaces Treated by Chemical Bath Deposition. *Appl. Surf. Sci.* **2011**, *256*, 4930–4933.
69. Kulinich, S. A.; Farzaneh, M. Effect of Contact Angle Hysteresis on Water Droplet Evaporation from Super-Hydrophobic Surfaces. *Appl. Surf. Sci.* **2009**, *255*, 4056–4060.
70. Chen, X.; Ma, R.; Li, J.; Hao, C.; Guo, W.; Luk, B. L.; Li, S. C.; Yao, S.; Wang, Z. Evaporation of Droplets on Superhydrophobic Surfaces: Surface Roughness and Small Droplet Size Effects. *Phys. Rev. Lett.* **2012**, *109*, 116101.
71. Fu, J.; Joshi, S. B.; Catchmark, J. M. A Study of Angular Effects in Focused Ion Beam Milling of Water Ice. *J. Micromech. Microeng.* **2008**, *18*, 095010.
72. Marko, M.; Hsieh, C.; Moberlychan, W.; Mannella, C. A.; Frank, J. Focused Ion Beam Milling of Vitreous Water: Prospects for an Alternative to Cryo-Ultramicrotomy of Frozen-Hydrated Biological Samples. *J. Microsc.* **2006**, *222*, 42–47.
73. Smith, N. S.; Skoczylas, W. P.; Kellogg, S. M.; Kinion, D. E.; Tesch, P. P.; Sutherland, O.; Aanesland, A.; Boswell, R. W. High Brightness Inductively Coupled Plasma Source for High Current Focused Ion Beam Applications. *J. Vac. Sci. Technol., A* **2006**, *24*, 2902–2906.
74. Nosonovsky, M.; Bhushan, B. Patterned Nonadhesive Surfaces: Superhydrophobicity and Wetting Regime Transitions. *Langmuir* **2007**, *24*, 1525–1533.
75. Anand, S.; Paxson, A. T.; Smith, J.; Dhiman, R.; Varanasi, K. K. Droplet Condensation and Growth on Nanotextured Surfaces Impregnated with an Immiscible Liquid. *Bull. Am. Phys. Soc.* **2012**, *57*, http://meetings.aps.org/link/BAPS.2012.MAR.X50.11.
76. Botman, A.; Mulders, J. J. L.; Hagen, C. W. Creating Pure Nanostructures from Electron-Beam-Induced Deposition Using Purification Techniques: A Technology Perspective. *Nanotechnology* **2009**, *20*, 372001.
77. Hejazi, V.; Nosonovsky, M. Wetting Transitions in Two-, Three-, and Four-Phase Systems. *Langmuir* **2011**, *28*, 2173–2180.
78. Certain commercial equipment, instruments, and materials are identified in this publication to adequately specify the experimental procedure. Such identification in no way implies approval, recommendation, or endorsement by NIST, nor does it imply that the equipment, instruments, or materials identified are necessarily the best available for the purpose.
79. Krylyuk, S.; Davydov, A. V.; Levin, I. Tapering Control of Si Nanowires Grown from $SiCl_4$ at Reduced Pressure. *ACS Nano* **2010**, *5*, 656–664.